



Cite this: *RSC Adv.*, 2023, **13**, 20342

Received 2nd May 2023  
 Accepted 5th June 2023

DOI: 10.1039/d3ra02894a  
[rsc.li/rsc-advances](http://rsc.li/rsc-advances)

## Photon avalanche assisted upconversion *via* customizing the green emission†

Manisha Prasad and Vineet Kumar Rai  \*

The developed  $\text{SnWO}_4$  phosphors incorporated with  $\text{Ho}^{3+}$ ,  $\text{Yb}^{3+}$  and  $\text{Mn}^{4+}$  ions have been explored under 980 nm laser irradiation. The molar concentration of dopants has been optimized to 0.5  $\text{Ho}^{3+}$ , 3.0  $\text{Yb}^{3+}$  and 5.0  $\text{Mn}^{4+}$  in  $\text{SnWO}_4$  phosphors. The upconversion (UC) emission from the codoped  $\text{SnWO}_4$  phosphors has been substantially amplified up to 13 times and described based on the energy transfer and charge compensation. On incorporating the  $\text{Mn}^{4+}$  ions in the  $\text{Ho}^{3+}/\text{Yb}^{3+}$  codoped system the sharp green luminescence shifted to reddish broadband emission due to the photon avalanche mechanism. The processes accountable for the concentration quenching have been described based on critical distance. The interaction responsible for the concentration quenching in  $\text{Yb}^{3+}$  sensitized  $\text{Ho}^{3+}$  and  $\text{Ho}^{3+}/\text{Mn}^{4+}$ : $\text{SnWO}_4$  phosphors is considered to be dipole-quadrupole and exchange interaction type, respectively. The activation energy 0.19 eV has been determined, and the phenomenon of thermal quenching is discussed using a configuration coordinate diagram.

## 1. Introduction

Manganese-based upconverting phosphors have recently been popular because of their extensive use in various promising applications, including solid-state lighting, displays, upconverters, temperature monitoring, plant growth and biological applications.<sup>1–3</sup> Manganese (Mn) can be utilized as an activator in downshifting (DS) and upconversion (UC) phenomena.<sup>4–6</sup> According to Blasse, the emission from  $\text{Mn}^{4+}$  lies in the deep red region, resulting from the  $^2\text{E} \rightarrow ^4\text{A}_2$  transition, which indicates that the  $\text{Mn}^{4+}$  incorporated phosphor can be a good candidate for red emission.<sup>7</sup> Mn is accepted as a single luminescence center and can be paired with other atoms such as Bi, Cr, and rare earths (RE) such as Ce, Pr, Dy, Sm, Yb, Ho, Nd, Er and Tm.<sup>8–18</sup> Researchers are interested in red-emitting  $\text{Mn}^{2+}/\text{Mn}^{4+}$  ions in aggregation with  $\text{Eu}^{3+}$  ions.<sup>19,20</sup> Codoping of manganese with lanthanide initiates a mutual energy transfer process, which enhances the photoluminescence properties. The production of dimers can sometimes improve the emission intensity.<sup>18</sup> The optical characteristics of Mn can be easily influenced by the oxidation state (*i.e.*, 2+, 4+) and the interaction of the crystal field. Besides the transition metals, fixed emissions can be obtained by doping the RE ions. On doping the lanthanides, the crystal field symmetry of the dopants breaks and due to the mixing of the  $4\text{f}^n$  and  $4\text{f}^{n-1}\text{5d}$  electronic

configurations having opposite parity, the electric dipole transitions become allowed.<sup>21–25</sup>

Among the various metal tungstates ( $\text{MWO}_4$ ),  $\text{SnWO}_4$  exists in two phases:  $\alpha$ - $\text{SnWO}_4$  is favoured at low synthesis temperature below 670 °C, whereas  $\beta$ - $\text{SnWO}_4$  is commonly obtained beyond this temperature.<sup>26</sup> The  $\text{SnWO}_4$  has a variety of applications, such as electrochemical performance, humidity sensing, photodynamic tumour therapy, photocatalytic degradation, water splitting, resistive switching memory, *etc.*<sup>27–30</sup> The  $\text{SnWO}_4$  is a diamagnetic semiconductor with a large bandgap and low phonon energy that can be employed for upconverting applications.<sup>26,27,31</sup>

In the present work,  $\text{Ho}^{3+}/\text{Yb}^{3+}/\text{Mn}^{4+}$ : $\text{SnWO}_4$  phosphors have been prepared and investigated through several characterization techniques such as X-ray diffraction (XRD), field emission scanning electron microscopy (FESEM), Fourier transform infrared spectroscopy (FTIR), Raman spectroscopy, X-ray photon spectroscopy (XPS), UV-vis-NIR spectroscopy and frequency upconversion study. In the coactivated system, the green emission of  $\text{Ho}^{3+}$  ions has been tuned with manganese ions. The detailed study of concentration quenching, the thermal stability and thermal quenching have been performed based on the UC measurements.

## 2. Experimentation

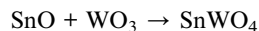
### 2.1 Synthesis of phosphors

A variety of  $\text{SnWO}_4$  phosphors at varying concentration of  $\text{Ho}^{3+}$ ,  $\text{Yb}^{3+}$  and  $\text{Mn}^{4+}$  ions have been produced using the conventional solid-state synthesis technique. All stoichiometric raw materials  $\text{SnO}_2$ ,  $\text{WO}_3$ ,  $\text{Ho}_2\text{O}_3$ ,  $\text{Yb}_2\text{O}_3$  and  $\text{MnO}_2$  were taken in high purity according to the following chemical expressions:

*Laser and Spectroscopy Laboratory, Department of Physics, Indian Institute of Technology (Indian School of Mines), Dhanbad, 826004, Jharkhand, India. E-mail: vineetkrrai@yahoo.co.in; vineetkrrai@iitm.ac.in; Tel: +91-326-223 5404/5282*

† Electronic supplementary information (ESI) available. See DOI: <https://doi.org/10.1039/d3ra02894a>

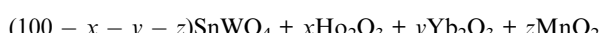




where,  $x = 0.1, 0.3, 0.5$  and  $0.7$  mol%



where,  $x = 0.5$ ;  $y = 1.0, 1.5, 3.0$  and  $4.0$  mol%



where,  $x = 0.5$ ;  $y = 3.0$ ;  $z = 1.0, 5.0, 10.0, 15.0$  and  $20.0$  mol%

The accurately weighing precursors were mixed in the mortar pestle. After grinding for 90 minutes using volatile liquid acetone, the mixture was maintained at  $1100$  °C in a muffle furnace for three hours. The phosphors were retrieved and used for additional characterizations after naturally cooling to ambient temperature.

## 2.2 Phosphors characterization

To determine the crystal formation and lattice parameters, the optimized  $\text{Ho}^{3+}/\text{Yb}^{3+}/\text{Mn}^{4+}:\text{SnWO}_4$  phosphors were analyzed by X-ray diffractometer in  $10^\circ \leq 2\theta \leq 70^\circ$  range. FESEM consisting of an airlock compartment has been used for surface morphological analysis and chemical components analyzed with EDAX. The vibrational bands have been detected with the FTIR and

Raman spectroscopy. XPS confirms the valence states and binding energies of the elements in phosphors. Diffuse reflectance spectra (DRS) have been monitored in the UV-vis-NIR region. The developed phosphors have been irradiated with a continuous wave laser source to achieve frequency UC. The monochromator used for this purpose consists of a triple grating and a photomultiplier tube. The luminescence lifetimes measurements have been carried out by using HORIBA 'Lifetime Spectrometer' and micro second xenon pulse lamp excitation. Thermal stability experiments have been carried out using a multimeter, thermocouple, and a small heater. Calculations of CIE coordinates have been performed using the GoCIE software.

## 3. Results and discussion

### 3.1 Structural characterization

**3.1.1. XRD analysis.** Fig. 1(a) displays the crystalline nature of the codoped  $\text{SnWO}_4$  phosphors. The diffraction patterns of phosphors are consistent with the JCPDS file 01-070-1497, of the  $\beta$ - $\text{SnWO}_4$  system.<sup>26</sup>  $\beta$ - $\text{SnWO}_4$  has a cubic structure with space group number 198 and space group  $\bar{P}\bar{1}23$ . The unit cell consists of  $\text{SnO}_6$  octahedra and  $[\text{WO}_4]^{2-}$  tetrahedra with lattice constant  $a = b = c = 7.2989$  Å,  $\alpha = \beta = \gamma = 90^\circ$ , volume =  $388.84$  Å<sup>3</sup>. According to the Debye–Scherrer equation, the crystallite size is given by,<sup>32</sup>

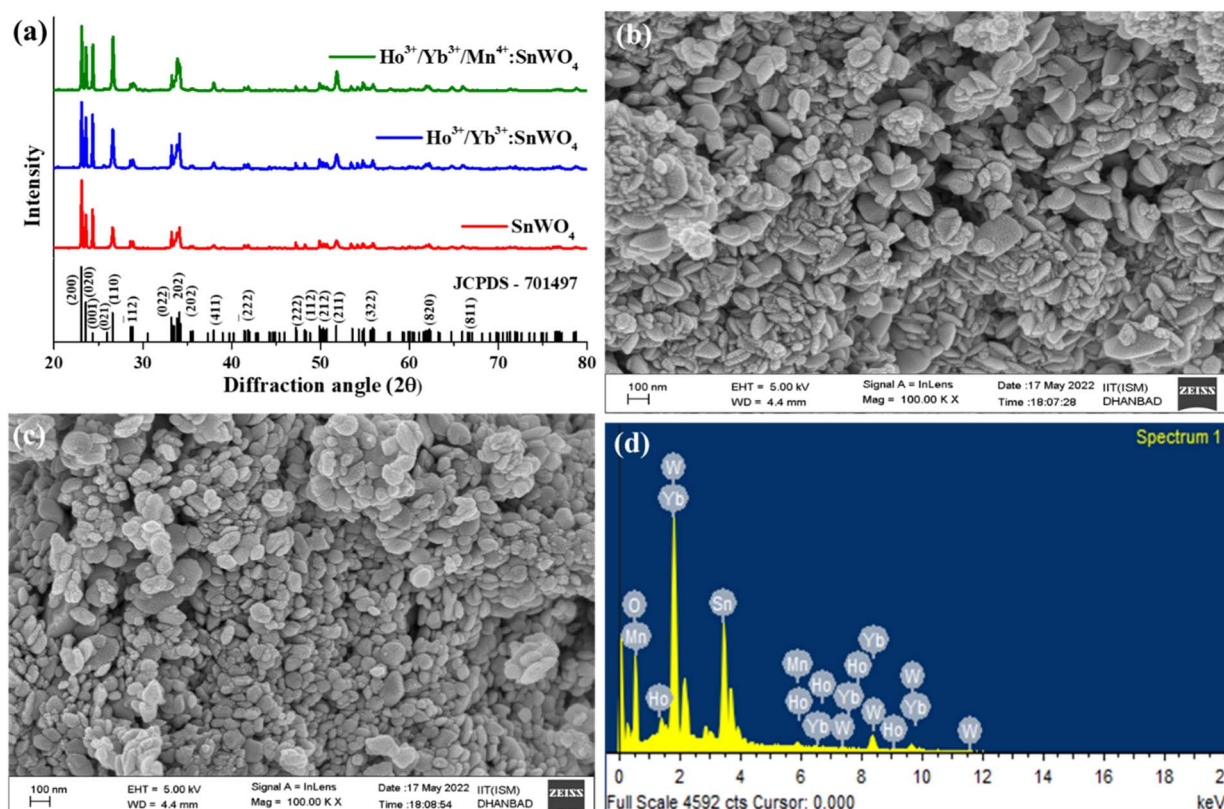


Fig. 1 (a) XRD spectra of  $\text{SnWO}_4$  host, optimized  $\text{Ho}^{3+}/\text{Yb}^{3+}$  and  $\text{Ho}^{3+}/\text{Yb}^{3+}/\text{Mn}^{4+}:\text{MgWO}_4$  phosphors. The FESEM images of (b)  $\text{Ho}^{3+}/\text{Yb}^{3+}$  (c)  $\text{Ho}^{3+}/\text{Yb}^{3+}/\text{Mn}^{4+}:\text{SnWO}_4$  phosphors. (d) EDAX of  $\text{Ho}^{3+}/\text{Yb}^{3+}/\text{Mn}^{4+}:\text{SnWO}_4$  phosphors.

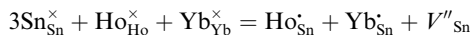
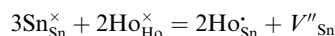
$$D = \frac{0.89\lambda}{\beta \cos \theta} \quad (1)$$

where 'λ' implies the wavelength of X-ray, 'β' designates the full width at half maxima and 'θ' denotes Bragg's diffraction angle. The estimated crystallite sizes for  $\text{SnWO}_4$ ,  $\text{Ho}^{3+}/\text{Yb}^{3+}:\text{SnWO}_4$  and  $\text{Ho}^{3+}/\text{Yb}^{3+}/\text{Mn}^{4+}:\text{SnWO}_4$  phosphors are determined to be 66.95 nm, 62.54 nm and 60.39 nm respectively. Further, the positive slope value obtained from the Williamson-Hall equation demonstrates the tensile strain created in the phosphors due to dopants ions.<sup>33</sup> The decrease in strain followed by the decrease in slope values (0.017, 0.016, 0.009) with codoping may be the reason for the decrease in crystallite size.<sup>32,34</sup>

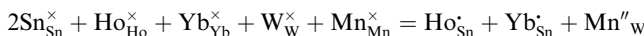
The absence of any extra peak in the developed phosphors, indicates that there is no impurity phase. The intense diffraction peaks present in the phosphors correspond to (200), (020), (001), (110), (112), (022), (202), (202), (411), (222), (222), (112), (212), (211), (322), (820) and (811) *hkl* planes.<sup>35</sup> Again, using relation between the radius of the host cation ' $R_m(\text{CN})$ ' and doped ion ' $R_d(\text{CN})$ ', the acceptable percent of doping ( $D_r$ ) can be confirmed as,<sup>32,34</sup>

$$D_r = 100 \times \frac{R_m(\text{CN}) - R_d(\text{CN})}{R_m(\text{CN})} \quad (2)$$

where the values of ionic radii for  $\text{Sn}^{2+}$ ,  $\text{W}^{6+}$ ,  $\text{Ho}^{3+}$ ,  $\text{Yb}^{3+}$  and  $\text{Mn}^{4+}$  are 0.69 Å, 0.60 Å, 0.90 Å, 0.86 Å, 0.53 Å in VI coordination, respectively.<sup>36</sup> The  $D_r$  value for  $\text{Sn}^{2+}$  and  $\text{Ho}^{3+}/\text{Yb}^{3+}$  is 30% and 24%, respectively. Also, for  $\text{W}^{6+}$  and  $\text{Mn}^{4+}$  ions, the  $D_r$  value is 11%. The calculated  $D_r$  values in the present case is less than 30%. This implies that the dopants successfully occupy the cationic sites of the host. The substitution of  $\text{Sn}^{2+}$  by the RE ions creates Sn vacancy in the prepared  $\text{Ho}^{3+}:\text{SnWO}_4$  and  $\text{Ho}^{3+}/\text{Yb}^{3+}:\text{SnWO}_4$  phosphors, due to which the  $\text{SnWO}_4$  system shows charge imbalance that can be demonstrated by using the following Kroger Vink notation given,<sup>6,34,37</sup>



The vacancy of oxygen ( $\text{W}_{\text{W}}^{\times} + \text{Mn}_{\text{Mn}}^{\times} = \text{Mn}''_{\text{W}} + V''_{\text{O}}$ ) in the  $\text{SnWO}_4$  sites is produced when  $\text{Mn}^{4+}$  is integrated into  $\text{SnWO}_4$  phosphors and  $\text{W}^{6+}$  is replaced by  $\text{Mn}^{4+}$ . Thus, it can be applied to the method described below to compensate the Sn vacancy  $V_{\text{Sn}}$ :



**3.1.2. FE-SEM and EDAX.** The FESEM images {Fig. 1(b) and (c)} show the morphological properties of prepared phosphors. The image taken on 100 nm scale shows that the particles are agglomerated on the surface. Additionally, particle size appears to be decreasing from  $\text{Ho}^{3+}/\text{Yb}^{3+}$  to  $\text{Ho}^{3+}/\text{Yb}^{3+}/\text{Mn}^{4+}:\text{SnWO}_4$  phosphors. The presence of all elements *viz.*, tin, tungsten, oxygen, holmium, ytterbium and manganese are confirmed by an elemental analysis using EDAX.

**3.1.3. FTIR and Raman analysis.** The vibrational features of the  $\text{SnWO}_4$  host have been accomplished using the FTIR spectrum over the 400–4000  $\text{cm}^{-1}$  range {Fig. 2(a)}. The phonon energy corresponds to the maxima at 604  $\text{cm}^{-1}$  and 668  $\text{cm}^{-1}$ . The asymmetric stretching bonds of the  $\text{WO}_6$  group are responsible for these vibrations. The peaks at 768  $\text{cm}^{-1}$  and 850  $\text{cm}^{-1}$  resemble the stretching vibration of W-W and W-O-W bonds. The stretching and bending mode of the hydroxyl ( $-\text{OH}$ ) group appears at 1634  $\text{cm}^{-1}$  and 3435  $\text{cm}^{-1}$ .<sup>35,38</sup>

Further, the developed phosphors have been characterized with Raman spectra in 100–1000  $\text{cm}^{-1}$  range {Fig. 2(b)}. The detected Raman peaks indicate that the cubic  $\beta$ -phase  $\text{SnWO}_4$  phosphors have been successfully formed. According to the group theory,  $\beta$ - $\text{SnWO}_4$  consists of 36 vibration peaks, 18 of them are Raman, and rest of them are infrared active. In Mulliken notation, it is given by 6A, 6E, 6E, 18T.<sup>27</sup> Several Raman shifts are detected at 135  $\text{cm}^{-1}$ , 275  $\text{cm}^{-1}$ , 327  $\text{cm}^{-1}$ , 718  $\text{cm}^{-1}$  and 807  $\text{cm}^{-1}$ .<sup>28</sup> The stretching vibration of W-O bonds in the  $\text{WO}_6$  octahedra appears at 718  $\text{cm}^{-1}$  and 807  $\text{cm}^{-1}$ .<sup>35</sup> The peak intensity decreases on doping  $\text{Ho}^{3+}/\text{Yb}^{3+}/\text{Mn}^{4+}$ , which shows the successful incorporation of dopants. When the dopants are added, the bond distance between two atoms decreases, and there is a reduction in the phonon excitation probability.<sup>39</sup>

**3.1.4. XPS analysis.** The chemical analysis and binding energy of the elements present in the codoped phosphors have been confirmed with XPS spectroscopy. The spectrum (binding energy *vs.* count per second) has been recorded from 0–1200 eV {Fig. 2(c)}. The XPS spectrum shows that all dopants and host elements (Ho, Yb, Mn, Sn, W and O) are present in the phosphors. The peak observed at ~284 eV due to C1s is used for binding energy calibration. The survey scan shows the characteristic peaks of Sn (4d) at 25 eV. The spin-orbit doublets are detected at 484 eV (3d<sub>5/2</sub>) and 495 eV (3d<sub>3/2</sub>).<sup>35</sup> Additionally, the 3p<sub>3/2</sub> and 3p<sub>1/2</sub> states are responsible for the peaks at 715 eV and 756 eV. The XPS peaks for tungsten are found at 35 eV (4f<sub>7/2</sub>), 247 eV (4d<sub>5/2</sub>), 259 eV (4d<sub>3/2</sub>), 426 eV (4p<sub>3/2</sub>) and 495 eV (4p<sub>1/2</sub>).<sup>6,40</sup> The XPS peaks of oxygen are observed at 21 eV (O2s), 530 eV (O 1s) and 974 eV (OKLL).<sup>6</sup> As the concentration of dopants is very low in the developed  $\text{SnWO}_4$  phosphors, the intensity of  $\text{Ho}^{3+}/\text{Yb}^{3+}/\text{Mn}^{4+}$  is comparatively small. The 4d<sub>3/2</sub> and 4d<sub>5/2</sub> orbitals are responsible for the binding energy maxima, which are positioned at 159 eV and 184 eV respectively and at 7 eV due to the Yb (4f<sub>5/2</sub>).<sup>5</sup> The +4-oxidation state of manganese has been identified with peaks at 642 eV and 654 eV. It corresponds to the 2p<sub>3/2</sub> and 2p<sub>1/2</sub> orbitals due to spin-orbit splitting.<sup>41</sup>

### 3.2 Optical characterization

**3.2.1. Diffuse reflectance spectra and bandgap analysis.** The  $\text{SnWO}_4$ , codoped  $\text{Ho}^{3+}/\text{Yb}^{3+}$  and  $\text{Ho}^{3+}/\text{Yb}^{3+}/\text{Mn}^{4+}:\text{SnWO}_4$  phosphors have been characterized with UV-vis spectroscopy to find the absorption bands in the 250–1250 nm wavelength range {Fig. 2(d)}. The spectra were calibrated with the standard  $\text{BaSO}_4$  powder. There is no absorption peak for the  $\text{SnWO}_4$  host. The doped/codoped  $\text{SnWO}_4$  phosphors consist of absorption peaks at 538 nm and 640 nm that correspond to the  ${}^5\text{I}_8 \rightarrow {}^5\text{F}_4$ ,  ${}^5\text{S}_2$  and  ${}^5\text{I}_8 \rightarrow {}^5\text{F}_5$  transitions. The 970 nm peak shows the  ${}^2\text{F}_{7/2}$



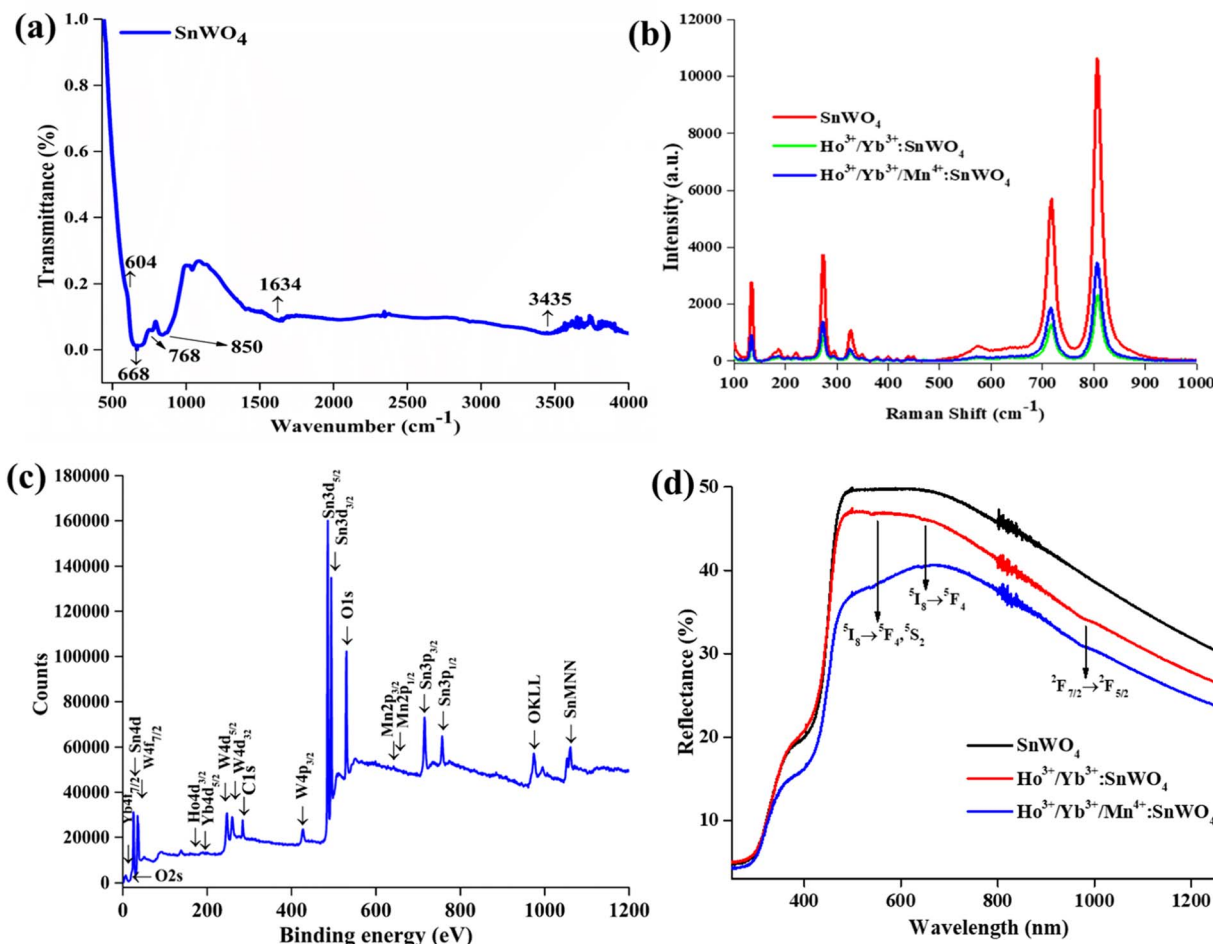


Fig. 2 (a) FTIR spectrum of  $\text{SnWO}_4$  host, (b) Raman spectra of  $\text{SnWO}_4$ ,  $\text{Ho}^{3+}/\text{Yb}^{3+}$  and  $\text{Ho}^{3+}/\text{Yb}^{3+}/\text{Mn}^{4+}:\text{SnWO}_4$  phosphors, (c) XPS of  $\text{Ho}^{3+}/\text{Yb}^{3+}/\text{Mn}^{4+}:\text{SnWO}_4$  phosphors (d) UV-vis spectra of  $\text{SnWO}_4$ ,  $\text{Ho}^{3+}/\text{Yb}^{3+}$  and  $\text{Ho}^{3+}/\text{Yb}^{3+}/\text{Mn}^{4+}:\text{SnWO}_4$  phosphors.

$\rightarrow ^2\text{F}_{5/2}$  absorption transition from  $\text{Yb}^{3+}$ . Applying the following relationship between the Kubelka Monk function and Tauc, the bandgap has been calculated from the DRS spectra,<sup>25</sup>

$$[F(R_\infty)h\nu] = C(h\nu - E_g)^n \quad (3)$$

where,  $F(R_\infty)$  stands for Kubelka–Munk function which satisfies the following relation,

$$F(R_\infty) = (1 - R)^2/2R = K/S \quad (4)$$

where 'R' stands for diffuse reflectance of the spectrum, 'K' stands for absorption coefficient and 'S' stands for scattering coefficient.  $F(R_\infty)$  depicts the reflection of the infinitely thick sample against a reference at each wavelength, 'C' is a constant, ' $h\nu$ ' stands for photon energy, ' $E_g$ ' for the bandgap and  $n = \frac{1}{2}$  for direct bandgap. The obtained values of bandgap are 3.60 eV, 3.54 eV and 3.66 eV, corresponding to  $\text{SnWO}_4$ ,  $\text{Ho}^{3+}/\text{Yb}^{3+}:\text{SnWO}_4$  and  $\text{Ho}^{3+}/\text{Yb}^{3+}/\text{Mn}^{4+}:\text{SnWO}_4$  phosphors, respectively. The results show that with the doping of larger atoms in the  $\text{Sn}^{2+}$  sites, the bandgap decreases, and with the smaller manganese doping, the bandgap increases.<sup>26,34</sup>

**3.2.2. Photoluminescence study and effect of  $\text{Mn}^{4+}$  codoping.** Fig. 3(a) displays the UC emission of produced phosphors in the spectral range of 350–900 nm after excitation at 980 nm radiation. The emission from doped/codoped  $\text{SnWO}_4$  phosphors has been enhanced by altering the concentration of  $\text{Ho}^{3+}$  (0.1, 0.3, 0.5 and 0.7 mol%)/ $\text{Yb}^{3+}$  (1.0, 1.5, 3.0 and 7.0 mol%)/ $\text{Mn}^{4+}$  (1.0, 5.0, 10.0, 15.0 and 20.0 mol%). The luminescence peaks found at  $\sim 541$  nm and  $\sim 645$  nm, arising from  $\text{Ho}^{3+}$  ions, are responsible due to the  $^5\text{F}_4$ ,  $^5\text{S}_2 \rightarrow ^5\text{I}_8$  and  $^5\text{F}_5 \rightarrow ^5\text{I}_8$  transitions, respectively. Codoping of  $\text{Yb}^{3+}$  ions enhanced the obtained UC emission intensity. Due to the  $\text{Yb}^{3+}$  ion's sensitizing effect, the green emission is intensified by 9 times that of  $\text{Ho}^{3+}:\text{SnWO}_4$  phosphors.

The UC emission intensity ( $I$ ) and pump power ( $p$ ) is correlated by the expression  $I \propto p^n$ , where  $n$  is the number of pump photons needed to populate the emitting levels. The calculated ' $n$ ' value for the  $^5\text{F}_4$ ,  $^5\text{S}_2 \rightarrow ^5\text{I}_8$  transition is 1.3. The decreased slope value in the  $\text{Ho}^{3+}/\text{Yb}^{3+}$  doped  $\text{SnWO}_4$  system is due to upconversion saturation at high power density, which is a consequence of the involvement of processes like energy transfer and non-radiative relaxation.<sup>42–44</sup> The energy level diagram has been used to explain excitation and emission

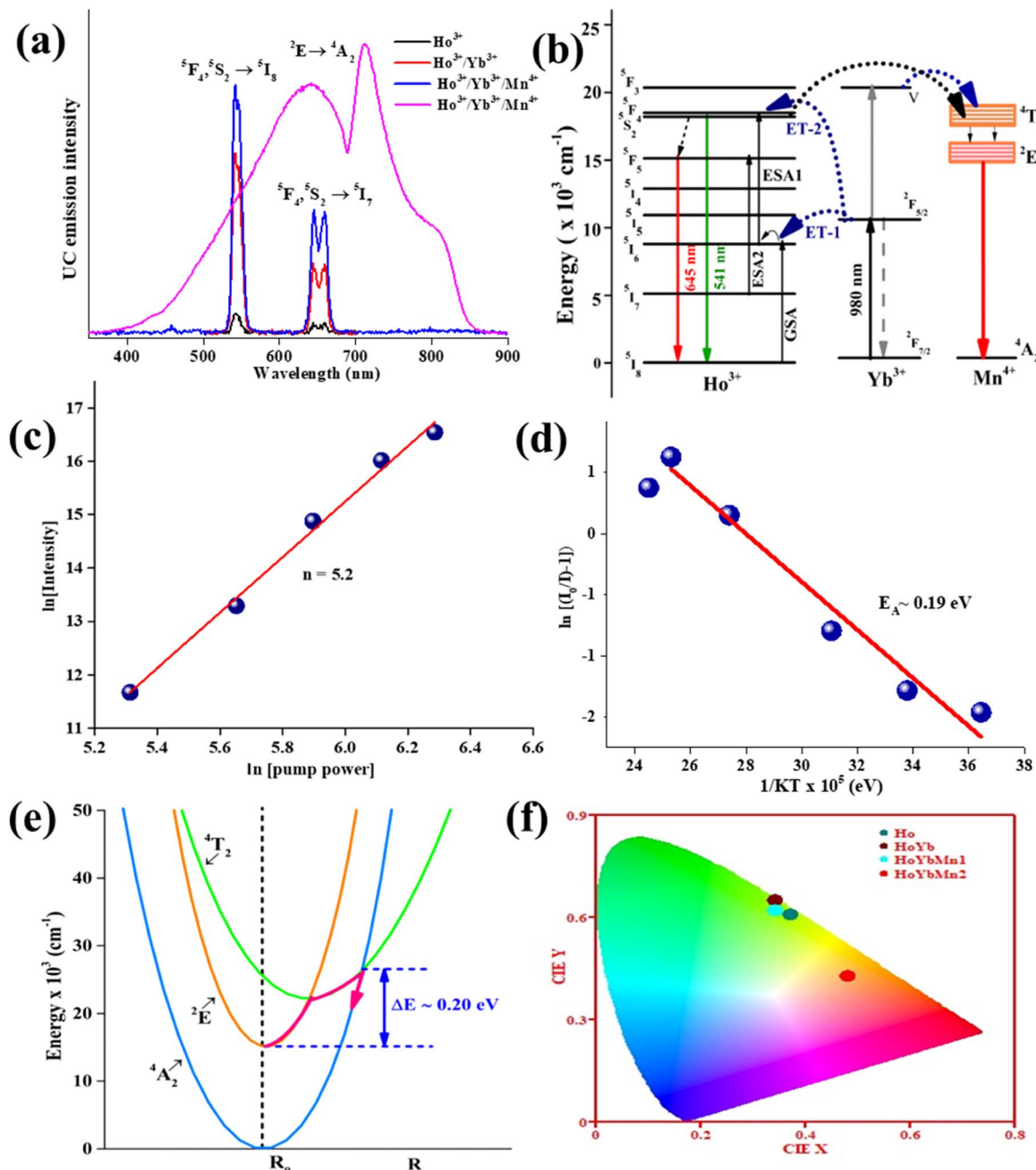


Fig. 3 (a) UC emission spectra of Ho<sup>3+</sup>, Ho<sup>3+</sup>/Yb<sup>3+</sup>, Ho<sup>3+</sup>/Yb<sup>3+</sup>/Mn<sup>4+</sup>:SnWO<sub>4</sub> phosphors upon 980 nm excitation, (b) schematic energy level diagram of Ho<sup>3+</sup>/Yb<sup>3+</sup>/Mn<sup>4+</sup> (c) slope value 'n' for broadband in Ho<sup>3+</sup>/Yb<sup>3+</sup>/Mn<sup>4+</sup>:SnWO<sub>4</sub> phosphors; (d) activation energy of Ho<sup>3+</sup>/Yb<sup>3+</sup>/Mn<sup>4+</sup>:SnWO<sub>4</sub> phosphors, (e) configuration coordinate diagrams showing thermal quenching in Ho<sup>3+</sup>/Yb<sup>3+</sup>/Mn<sup>4+</sup>:SnWO<sub>4</sub> phosphors (f) CIE coordinates for Ho<sup>3+</sup>, Ho<sup>3+</sup>/Yb<sup>3+</sup>, Ho<sup>3+</sup>/Yb<sup>3+</sup>/Mn<sup>4+</sup>:SnWO<sub>4</sub> phosphors.

mechanisms of the Ho<sup>3+</sup>, Yb<sup>3+</sup> and Mn<sup>4+</sup> dopants in SnWO<sub>4</sub> {Fig. 3(b)}. The luminescence from Ho<sup>3+</sup>/Yb<sup>3+</sup> is the result of ESA, GSA and ET processes.<sup>5,45,46</sup> The electrons are stimulated to the <sup>5</sup>I<sub>6</sub> level by taking the 980 nm excitation energy through GSA, and the <sup>5</sup>F<sub>4</sub>, <sup>5</sup>S<sub>2</sub> levels of Ho<sup>3+</sup> ions are then populated by absorbing the second photon (ESA1). Again, the <sup>5</sup>F<sub>4</sub> and <sup>5</sup>S<sub>2</sub> levels are populated by the energy transfer from Yb<sup>3+</sup> ions through ET-1 and ET-2 processes. The <sup>5</sup>F<sub>4</sub>, <sup>5</sup>S<sub>2</sub> → <sup>5</sup>I<sub>8</sub> transition results in the green emission at 541 nm. A part of the population at <sup>5</sup>F<sub>4</sub>, <sup>5</sup>S<sub>2</sub> levels relaxes non-radiatively (involving 5 phonons) to

populate the next lower <sup>5</sup>F<sub>5</sub> level. Also, the ESA2 from the <sup>5</sup>I<sub>6</sub> level populates the <sup>5</sup>F<sub>5</sub> level from where the <sup>5</sup>F<sub>5</sub> → <sup>5</sup>I<sub>8</sub> transition corresponding to the red emission at 645 nm occurs.

Further, on introducing the Mn<sup>4+</sup> ions in the Ho<sup>3+</sup>/Yb<sup>3+</sup>:SnWO<sub>4</sub> phosphors, some fascinating results have been obtained. Here, Mn<sup>4+</sup> acts as an intensity enhancer at low pump photon density and a spectra modifier on tuning the pump power density. In the phosphors, after codoping Mn<sup>4+</sup>, the UC emission intensity of the green band is enhanced by 1.4 times and 13 times compared to the Ho<sup>3+</sup>/Yb<sup>3+</sup> and Ho<sup>3+</sup>, respectively. On increasing the pump



power ( $<23.6 \text{ W cm}^{-2}$ ) the UC emission intensity enhances, and at higher pump power ( $\geq 23.6 \text{ W cm}^{-2}$ ) there is a change in the sharp UC peak to broadband ranging from 400–900 nm due to the  $^2\text{E} \rightarrow ^4\text{A}_2$  transition. At  $45.1 \text{ W cm}^{-2}$  visible broadband occurs, and the intensity goes on increasing on a further increase of pump power density. The broadband emitting  $\text{Ho}^{3+}/\text{Yb}^{3+}/\text{Mn}^{4+}:\text{SnWO}_4$  phosphors is found with slope value 5.2 {Fig. 3(c)}, demonstrating the role of the photon avalanche (PA), which is supported by the cross-relaxation process.<sup>47–51</sup> The single  $\text{Mn}^{4+}:\text{SnWO}_4$  is not excited with 980 nm excitation because there is no equivalent energy level. Hence, the energy transfer from either  $\text{Ho}^{3+}$  or  $\text{Yb}^{3+}$  or both is the only possible way to populate the energy levels of  $\text{Mn}^{4+}$ . The energy transfer from  $\text{Ho}^{3+}/\text{Yb}^{3+}$  ions to ground state  $^4\text{A}_2$  of  $\text{Mn}^{4+}$  becomes prominently active when the pump photon number increases sufficiently. The two photons trigger other two-photons and further to four and sixteen photons and so on, simultaneously for a photon avalanche process, which populates the excited  $^4\text{T}_2$  level of  $\text{Mn}^{4+}$ .  $\text{Mn}^{4+}$  ions are populated in the  $^2\text{E}$  level through the non-radiative relaxation from the  $^4\text{T}_2$  level. Owing to the ligand field dependency of  $\text{Mn}^{4+}$  ions, the broadband spectra corresponding to the  $^2\text{E} \rightarrow ^4\text{A}_2$  transition has two overlapped peaks at 640 and 710 nm, which is located in the red and deep red region. The peak at 710 nm arises in the broad spectra because of the simultaneous generation and annihilation of phonons caused by the electronic states of 3d electrons and lattice vibrations.<sup>52–56</sup>

To further reveal the spectroscopic properties, the luminescence lifetimes measurements of  $\text{Ho}^{3+}/\text{Yb}^{3+}$  and  $\text{Ho}^{3+}/\text{Yb}^{3+}/\text{Mn}^{4+}:\text{SnWO}_4$  phosphors have been performed upon 361 nm excitation. The ESI Fig. S(a) and S(b)† show the rise and decay time of green (530 nm) and red (645 nm) emissions corresponding to the  $^5\text{F}_4, ^5\text{S}_2 \rightarrow ^5\text{I}_8$  and  $^5\text{F}_5 \rightarrow ^5\text{I}_8$  transitions, respectively, in  $\text{Ho}^{3+}/\text{Yb}^{3+}$  and  $\text{Ho}^{3+}/\text{Yb}^{3+}/\text{Mn}^{4+}:\text{SnWO}_4$  phosphors. The decay curves are fitted to the exponential rise and decay function given by  $[I = I_0[\exp(-) - \exp(-t/\tau_d)]]$  where ' $I$ ' and ' $I_0$ ' are emission intensity at time ' $t$ ' and '0', ' $\tau_r$ ', ' $\tau_d$ ' are the rise and decay times.<sup>57–59</sup> The rise time is found to be  $0.92 \mu\text{s}$  and  $1.41 \mu\text{s}$  for green emission and  $0.73 \mu\text{s}$  and  $1.12 \mu\text{s}$  for red emission for  $\text{Ho}^{3+}/\text{Yb}^{3+}$  and  $\text{Ho}^{3+}/\text{Yb}^{3+}/\text{Mn}^{4+}:\text{SnWO}_4$  phosphors. The decay time for  $\text{Ho}^{3+}/\text{Yb}^{3+}$  and  $\text{Ho}^{3+}/\text{Yb}^{3+}/\text{Mn}^{4+}:\text{SnWO}_4$  phosphors are found to be  $5.83 \mu\text{s}$  and  $5.79 \mu\text{s}$  for green emission and  $5.75 \mu\text{s}$  and  $5.81 \mu\text{s}$  for red emission, respectively. There is a slight change in decay time has been observed. The decay time is the lifetime of the excited levels of the rare earth ions involved in the emission process. However, there is an increase in rise time for both 530 nm and 645 nm emissions has been observed, which shows an increment in the efficient energy transfer process among the dopant ions.

**3.2.3. Concentration quenching and energy transfer interaction.** On increasing the percentage of activator ions beyond 0.5 mole percent of  $\text{Ho}^{3+}$  and 5.0 mole percent of  $\text{Mn}^{4+}$  the decrease in luminescence intensity is recorded. Because the distance among dopant ions becomes smaller, and the sensitizers ions are insufficient to transfer the energy to such a smaller distance. In the  $\text{Ho}^{3+}/\text{Yb}^{3+}:\text{SnWO}_4$  phosphors, the mean distance among  $\text{Ho}^{3+}$  ions have a significant influence on the energy transfer between them. As a result, the critical distance has been calculated using the Blesse equation,<sup>54</sup>

$$R_c = 2 \left[ \frac{3V}{4\pi X_c N} \right]^{1/3} \quad (5)$$

where 'V' stands for unit cell volume, ' $X_c$ ' for critical concentration, and 'N' for the quantity of activator ions occupying each lattice site. In present case,  $V = 388.84 \text{ \AA}^3$ ,  $X_c$  is 0.5 mol%,  $N = 4$ . After calculation, the  $R_c$  value is found to be  $7.18 \text{ \AA}$ . If  $R_c$  is more than 5, it means that rare earth interactions are not the result of exchange interactions.<sup>34,46</sup> Hence, the multipolar interaction precedes the mechanism, which may be established by the relationship given by Dexter and Van Uitert,<sup>60</sup>

$$\frac{I}{C} = K [1 + \beta C^{Q/3}]^{-1} \quad (6)$$

where ' $I$ ' stands for the emission intensity corresponding to each concentration and ' $C$ ' stands for the dopant ion concentration. ' $K$ ' and ' $\beta$ ' are constants, while ' $Q$ ' denotes the nature of the interaction between the quenching center and luminescence center. The exchange interaction, electric dipole–dipole, electric dipole–quadrupole, and electric quadrupole–quadrupole interactions are represented by the distinct values of ' $Q$ ' = 3, 6, 8, and 10. Since the value of  $Q/3$  has been determined to be 2.60,  $Q$  is roughly equivalent to 8. This implied that the concentration quenching of  $\text{Ho}^{3+}$  ions in the  $\text{SnWO}_4$  phosphors is caused by electric dipole–quadrupole interaction.<sup>53,61</sup> However, by considering the concentration of  $\text{Mn}^{4+}$  ions, the energy transfer process from  $\text{Ho}^{3+}$  to  $\text{Mn}^{4+}$  can be identified. The found value of  $R_c$  is  $3.2 \text{ \AA}$ , which is less than  $5 \text{ \AA}$ . This shows that  $\text{Ho}^{3+}$  transfers energy to  $\text{Mn}^{4+}$  via short range exchange interaction in the  $\text{Ho}^{3+}/\text{Yb}^{3+}/\text{Mn}^{4+}:\text{SnWO}_4$  phosphors.<sup>62</sup> The efficient energy migration is decided by the critical distance. It becomes important as the dopant's concentration increases. Beyond the critical concentration, further increase in the dopant's concentration brings the dopants too close (*i.e.*, below critical distance) and the attractive potential rises. The obtained value of critical distance confirms that at high concentration (5.0 mol%  $\text{Mn}^{4+}$ ), *i.e.*, when there is a small distance between  $\text{Mn}^{4+}$  ions, the excitation energy effectively moves among  $\text{Mn}^{4+}$  ions till it hits a killing site and then decays non-radiatively. Thus, the concentration quenching decreases the UC emission intensity.

**3.2.4. Thermal stability, configuration coordinates and CIE diagram.** The temperature dependent UC spectra of  $\text{Ho}^{3+}/\text{Yb}^{3+}/\text{Mn}^{4+}:\text{SnWO}_4$  phosphors have been recorded over 303–473 K temperature range to determine the thermal stability. Temperature is a measurable parameter that controls the dynamics of the UC process. Thus, it becomes necessary to check any optical behavior change, such as spectral position, lifetime, CIE, CCT, *etc.*, before the device fabrication. As temperature increases, the intensity of UC emission decreases to 46% at 423 K compared to the initial intensity.<sup>5,6,62–65</sup> Thermal quenching at higher temperatures is because of the non-radiative multiphonon relaxation caused by lattice vibrations. The relevant relation between phonon density ( $n$ ), energy gap ( $\hbar\omega$ ), Boltzmann constant ( $K$ ) and the absolute temperature ( $T$ ) can be given by equation  $\langle n \rangle = 1 / \left[ 1 - \left( \frac{\hbar\omega}{KT} \right) \right]$ .<sup>5,53</sup> The activation energy can be determined by using the following Arrhenius equation,<sup>58,66</sup>



$$I = \frac{I_0}{1 + C \exp\left(-\frac{E_A}{kT}\right)} \quad (7)$$

The calculated value of activation energy  $E_A$  for the broad emitting  $\text{Ho}^{3+}/\text{Yb}^{3+}/\text{Mn}^{4+}:\text{SnWO}_4$  phosphors is 0.19 eV {Fig. 3(d)}. Greater the activation energy of phosphors, more is the thermal stability. The activation energy and thermal quenching due to increased temperature can be illustrated by using the configuration coordinate {Fig. 3(e)}. The figure shows the  $^4\text{A}_2$ ,  $^2\text{E}$  and  $^4\text{T}_2$  energy level parabola in terms of potential curve equilibrium position or internuclear distance ( $R$ ). According to the configuration coordinate, the parabolas of  $^4\text{A}_2$  and  $^2\text{E}$  energy states do not cross each other. Thus, the quenching of UC intensity is not possible through  $^4\text{A}_2$  and  $^2\text{E}$  crossover. With an increase in temperature, thermal quenching is caused by the wide splitting of the  $^4\text{T}_2$  and  $^4\text{T}_1$  spin-quartet states of  $\text{Mn}^{4+}$ . As a result, there is horizontal displacement of the  $^4\text{T}_2$  parabola. The  $^2\text{E}$ ,  $^2\text{T}_1$ ,  $^2\text{T}_2$  and  $^4\text{A}_2$  levels are originated from the same  $t_2^3$  electronic orbital and the  $^4\text{T}_1$  and  $^4\text{T}_2$  levels are formed from another  $t_2^2$  orbital. Therefore, the ground state  $^4\text{A}_2$  and excited state  $^4\text{T}_2$  (or  $^4\text{T}_1$ ) parabolas exhibit a significant lateral displacement. A greater displacement indicates a more intense electron-phonon interaction.<sup>67</sup> The lowest sublevel originating from the  $^4\text{T}_2$  state is shifted nearer to the emitting  $^2\text{E}$  state; due to that, the nonradiative transitions from  $^2\text{E}$  to  $^4\text{T}_2$  are promoted, which probably returns to the  $^4\text{A}_2$  ground state.<sup>68</sup> Thus, thermal quenching occurs in the phosphors owing to thermally generated crossover from the  $^4\text{T}_2$  excited state to the  $^4\text{A}_2$  ground state.

To visualize the color emission, the CIE coordinates of all developed phosphors have been determined {Fig. 3(f)}. The found CIE coordinates are (0.37, 0.61), (0.34, 0.65), (0.34, 0.62) and (0.48, 0.43) for  $\text{Ho}^{3+}$ ,  $\text{Ho}^{3+}/\text{Yb}^{3+}$ ,  $\text{Ho}^{3+}/\text{Yb}^{3+}/\text{Mn}^{4+}$  and broad emitting  $\text{Ho}^{3+}/\text{Yb}^{3+}/\text{Mn}^{4+}$  codoped  $\text{SnWO}_4$  phosphors, respectively. The observation shows that upon  $\text{Yb}^{3+}$  ions codoping in  $\text{Ho}^{3+}:\text{SnWO}_4$  phosphors, the CIE coordinates shifted towards a more greenish region, *i.e.*, the incorporation of  $\text{Yb}^{3+}$  enhances the purity. However, due to the codoping of  $\text{Mn}^{4+}$ , the CIE coordinates shift towards reddish region. Also, the CCT values have been calculated for all the phosphors, and the calculated values are 4937 K, 5403 K, 5395 K and 2579 K, respectively. The observation shows that from single  $\text{Ho}^{3+}$  doped to  $\text{Ho}^{3+}/\text{Yb}^{3+}/\text{Mn}^{4+}$  codoped phosphors, the CCT value shifted from cool light to warm light region.<sup>69</sup> Thus, the present phosphors can be used in green and broad visible upconverters.

## 4. Conclusion

The green and broad emitting  $\text{Ho}^{3+}/\text{Yb}^{3+}/\text{Mn}^{4+}:\text{SnWO}_4$  phosphors synthesized effectively by the solid-state reaction approach have been structurally and optically studied. Charge compensation boosted the green emission of  $\text{Ho}^{3+}$  in codoped  $\text{SnWO}_4$  phosphors by 13 times after incorporating  $\text{Mn}^{4+}$  ions. The broad UC emission is induced by the photon avalanche energy transfer process. Critical distance has been used to demonstrate the concentration quenching owing to exchange

interaction in the  $\text{Ho}^{3+}/\text{Yb}^{3+}/\text{Mn}^{4+}:\text{SnWO}_4$  phosphors. The temperature-dependent luminescence quenching of the broad emitting  $\text{Ho}^{3+}/\text{Yb}^{3+}/\text{Mn}^{4+}:\text{SnWO}_4$  phosphors has been described by using a configuration coordinate diagram. From these above experimental investigations, it can be inferred that the generated phosphors may be utilized for broadband visible optical devices.

## Conflicts of interest

There are no conflicts to declare.

## Acknowledgements

Ms Manisha Prasad is thankful to IIT(ISM), Dhanbad for providing the research fellowship.

## References

- 1 H. D. Nguyen and R. S. Liu, Narrow-band red-emitting  $\text{Mn}^{4+}$ -doped hexafluoride phosphors: synthesis, optoelectronic properties, and applications in white light-emitting diodes, *J. Mater. Chem. C*, 2016, **4**, 10759–10775.
- 2 M. Prasad and V. K. Rai, Frequency Upconversion in UCNPs Containing Transition Metal Ions, *Upconverting Nanoparticles: From Fundamentals to Applications*, 2022, pp. 141–169.
- 3 R. Cao, F. Zhang, C. Cao, X. Yu, A. Liang, S. Guo and H. Xue, Synthesis and luminescence properties of  $\text{CaAl}_2\text{O}_4:\text{Mn}^{4+}$  phosphor, *Opt. Mater.*, 2014, **38**, 53–56.
- 4 X. Xu, J. Ren, N. Huang, H. Zeng, G. Chen, D. Kong and H. Tao, Broadly tunable emission from Mn-doped zinc gallogermanate phosphors through composition modification, *Opt. Mater. Express*, 2014, **4**, 2433–2440.
- 5 M. Prasad and V. K. Rai, Influence of transition metal ions: Broad band upconversion emission in thermally stable phosphors, *J. Alloys Compd.*, 2020, **837**, 155289.
- 6 M. Prasad and V. K. Rai, Simultaneous effects of synthesis temperature and dopants on  $\text{MgWO}_4$  UC phosphors, *Methods Appl. Fluoresc.*, 2022, **10**, 034004.
- 7 L. Dong, L. Zhang, Y. Jia, Y. Xu, S. Yin and H. You,  $\text{ZnGa}_{2-y}\text{Al}_y\text{O}_4:\text{Mn}^{2+}, \text{Mn}^{4+}$  Thermochromic Phosphors: Valence State Control and Optical Temperature Sensing, *Inorg. Chem.*, 2020, **59**, 15969–15976.
- 8 L. Dong, L. Zhang, Y. Jia, B. Shao, W. Lü, S. Zhao and H. You, Site occupation and luminescence of novel orange-red  $\text{Ca}_3\text{M}_2\text{Ge}_3\text{O}_{12}:\text{Mn}^{2+}, \text{Mn}^{4+}$  ( $\text{M} = \text{Al}, \text{Ga}$ ) phosphors, *ACS Sustainable Chem. Eng.*, 2020, **8**, 3357–3366.
- 9 H. Zhou, N. Guo, M. Zhu, J. Li, Y. Miao and B. Shao, Photoluminescence and ratiometric optical thermometry in  $\text{Mn}^{4+}/\text{Eu}^{3+}$  dual-doped phosphor via site-favorable occupation, *J. Lumin.*, 2020, **224**, 117311.
- 10 L. Li, Y. Pan, Z. Chen, S. Huang and M. Wu, Tunable luminescence and energy transfer properties of  $\text{Bi}^{3+}$  and  $\text{Mn}^{4+}$  co-doped  $\text{Ca}_{14}\text{Al}_{10}\text{Zn}_6\text{O}_{35}$  phosphors for agricultural applications, *RSC Adv.*, 2017, **7**, 14868–14875.



11 H. Zhang, Y. Chen, X. Zhu, K. Liu, H. Zhou, X. Sun, Y. Feng, *et al.* The deep red  $\text{Ca}_2\text{YZr}_2\text{Al}_3\text{O}_{12}$ :  $\text{Mn}^{4+}$  phosphor and enhanced emission by  $\text{Bi}^{3+}$  doping, *J. Lumin.*, 2021, **236**, 118131.

12 Q. Sai, C. Xia, H. Rao, X. Xu, G. Zhou and P. Xu, Mn, Cr-co-doped  $\text{MgAl}_2\text{O}_4$  phosphors for white LEDs, *J. Lumin.*, 2011, **131**, 2359–2364.

13 X. Zhang and M. Gong, Single-phased white-light-emitting  $\text{NaCaBO}_3$ :  $\text{Ce}^{3+}$ ,  $\text{Tb}^{3+}$ ,  $\text{Mn}^{2+}$  phosphors for LED applications, *Dalton Trans.*, 2014, **43**, 2465–2472.

14 W. Liang and Y. Wang, Energy transfer between  $\text{Pr}^{3+}$  and  $\text{Mn}^{2+}$  in  $\text{K}_2\text{YZr}(\text{PO}_4)_3$ : Pr, Mn phosphor, *Mater. Chem. Phys.*, 2011, **127**, 170–173.

15 X. Qu, L. Cao, W. Liu, G. Su and P. Wang, Luminescence properties of  $\text{CdSiO}_3$ :  $\text{Mn}^{2+}$ ,  $\text{RE}^{3+}$  ( $\text{RE} = \text{Sm, Dy, Eu}$ ) phosphors, *J. Alloys Compd.*, 2009, **487**, 387–390.

16 R. Valiente, O. S. Wenger and H. U. Güdel, Near-infrared-to-visible photon upconversion process induced by exchange interactions in  $\text{Yb}^{3+}$ -doped  $\text{RbMnCl}_3$ , *Phys. Rev. B: Condens. Matter Mater. Phys.*, 2001, **63**, 165102.

17 Z. T. Chen, E. H. Song, M. Wu, S. Ding, S. Ye and Q. Y. Zhang, Bidirectional energy transfer induced single-band red upconversion emission of  $\text{Ho}^{3+}$  in  $\text{KZnF}_3$ :  $\text{Mn}^{2+}$ ,  $\text{Yb}^{3+}$ ,  $\text{Ho}^{3+}$  nanocrystals, *J. Alloys Compd.*, 2016, **667**, 134–140.

18 Y. Lv, Y. Jin, T. Sun, J. Su, C. Wang, G. Ju, Y. Hu, *et al.* Visible to NIR down-shifting and NIR to visible upconversion luminescence in  $\text{Ca}_{14}\text{Zn}_6\text{Ga}_{10}\text{O}_{35}$ :  $\text{Mn}^{4+}$ ,  $\text{Ln}^{3+}$  ( $\text{Ln} = \text{Nd, Yb, Er}$ ), *Dyes Pigm.*, 2019, **161**, 137–146.

19 J. Liao, Q. Wang, H. R. Wen, H. Yuan, S. J. Liu, J. Fu and B. Qiu, First observation of mutual energy transfer of  $\text{Mn}^{4+}$ – $\text{Er}^{3+}$  via different excitation in  $\text{Gd}_2\text{ZnTiO}_6$ :  $\text{Mn}^{4+}$ – $\text{Er}^{3+}$  phosphors, *J. Mater. Chem. C*, 2017, **5**, 9098–9105.

20 E. H. Song, S. Ding, M. Wu, S. Ye, Z. T. Chen, Y. Y. Ma and Q. Y. Zhang, Tunable white upconversion luminescence from  $\text{Yb}^{3+}$ – $\text{Tm}^{3+}$ – $\text{Mn}^{2+}$  tri-doped perovskite nanocrystals, *Opt. Mater. Express*, 2014, **4**, 1186–1196.

21 X. Qin, X. Liu, W. Huang, M. Bettinelli and X. Liu, Lanthanide-activated phosphors based on 4f-5d optical transitions: theoretical and experimental aspects, *Chem. Rev.*, 2017, **117**, 4488–4527.

22 K. Ogasawara, S. Watanabe, Y. Sakai, H. Toyoshima, T. Ishii, M. G. Brik and I. Tanaka, Calculations of complete 4f<sup>n</sup> and 4f<sup>n-1</sup> 5d<sup>1</sup> energy level schemes of free trivalent rare-earth ions, *Jpn. J. Appl. Phys.*, 2004, **43**, L611.

23 I. Gupta, S. Singh, S. Bhagwan and D. Singh, Rare earth (RE) doped phosphors and their emerging applications: A review, *Ceram. Int.*, 2021, **47**, 19282–19303.

24 G. Liu, Advances in the theoretical understanding of photon upconversion in rare-earth activated nanophosphors, *Chem. Soc. Rev.*, 2015, **44**, 1635–1652.

25 M. Prasad and V. K. Rai, Thermally stable upconverting  $\text{Na}_3\text{Zr}_2(\text{SiO}_4)_2\text{PO}_4$ :  $\text{Er}^{3+}$ – $\text{Yb}^{3+}$  phosphors for displays and optical thermometry, *J. Alloys Compd.*, 2022, **911**, 164968.

26 W. Jeitschko and A. W. Sleight, Synthesis, properties and crystal structure of  $\beta$ - $\text{SnWO}_4$ , *Acta Crystallogr., Sect. B: Struct. Crystallogr. Cryst. Chem.*, 1972, **28**, 3174–3178.

27 J. L. Solis, J. Frantti, V. Lantto, L. Häggström and M. Wikner, Characterization of phase structures in semiconducting  $\text{SnWO}_4$  powders by Mössbauer and Raman spectroscopies, *Phys. Rev. B: Condens. Matter Mater. Phys.*, 1998, **57**, 13491.

28 F. A. Alharthi, M. A. Alsaiari, M. S. Jalalah, M. Shashank, A. A. Alghamdi, J. S. Algethami and N. Ganganagappa, Combustion synthesis of  $\beta$ - $\text{SnWO}_4$ -rGO: Anode material for Li-ion battery and photocatalytic dye degradation, *Ceram. Int.*, 2021, **47**, 10291–10300.

29 C. Seidl, J. Ungelenk, E. Zittel, T. Bergfeldt, J. P. Sleeman, U. Schepers and C. Feldmann, Tin tungstate nanoparticles: a photosensitizer for photodynamic tumor therapy, *ACS Nano*, 2016, **10**, 3149–3157.

30 P. Han, B. Sun, S. Cheng, F. Yu, B. Jiao and Q. Wu, An optoelectronic resistive switching memory behavior of  $\text{Ag}/\alpha\text{-SnWO}_4/\text{FTO}$  device, *J. Alloys Compd.*, 2016, **681**, 516–521.

31 M. Zhang, Z. Cui, R. Song, B. Lv, Z. Tang, X. Meng, W. Bu, *et al.*  $\text{SnWO}_4$ -based nanohybrids with full energy transfer for largely enhanced photodynamic therapy and radiotherapy, *Biomaterials*, 2018, **155**, 135–144.

32 L. Mukhopadhyay, V. K. Rai, R. Bokolia and K. Sreenivas, 980 nm excited  $\text{Er}^{3+}$ – $\text{Yb}^{3+}$ – $\text{Li}^{+}$ – $\text{Ba}^{2+}$ :  $\text{NaZnPO}_4$  upconverting phosphors in optical thermometry, *J. Lumin.*, 2017, **187**, 368–377.

33 P. Ghosh, J. Oliva, E. D. L. Rosa, K. K. Haldar, D. Solis and A. Patra, Enhancement of upconversion emission of  $\text{LaPO}_4$ :  $\text{Er}@\text{Yb}$  core–shell nanoparticles/nanorods, *J. Phys. Chem. C*, 2008, **112**, 9650–9658.

34 S. Pattnaik and V. K. Rai, Impact of charge compensation on optical and thermometric behaviour of titanate phosphors, *Mater. Res. Bull.*, 2020, **125**, 110761.

35 S. R. Ede and S. Kundu, Microwave synthesis of  $\text{SnWO}_4$  nanoassemblies on DNA scaffold: a novel material for high performance supercapacitor and as catalyst for butanol oxidation, *ACS Sustainable Chem. Eng.*, 2015, **3**, 2321–2336.

36 R. D. Shannon, Revised effective ionic radii and systematic studies of interatomic distances in halides and chalcogenides, *Acta Crystallogr., Sect. A: Cryst. Phys., Diff., Theor. Gen. Crystallogr.*, 1976, **32**, 751–767.

37 S. Wang, Y. J. Han, L. Shi, M. X. Jia, Y. L. Tong, N. N. Bao, S. L. Niu, *et al.* Charge compensation assisted enhanced photoluminescence derived from  $\text{Al}^{3+}$ -codoped  $\text{NaLaMgWO}_6$ :  $\text{Mn}^{4+}$  phosphors for plant growth lighting applications, *J. Lumin.*, 2020, **226**, 117438.

38 H. N. Sumedha, M. A. Alsaiari, M. S. Jalalah, M. Shashank, F. A. Alharthi, N. Ahmad, N. Ganganagappa, *et al.* Rapid Microwave Synthesis of  $\beta$ - $\text{SnWO}_4$  Nanoparticles: An Efficient Anode Material for Lithium Ion Batteries, *Crystals*, 2021, **11**, 334.

39 T. Badapanda, V. Senthil, S. Panigrahi and S. Anwar, Diffuse phase transition behavior of dysprosium doped barium titanate ceramic, *J. Electroceram.*, 2013, **31**, 55–60.

40 S. Wang, H. Gao, C. Chen, Q. Li, C. Li, Y. Wei and L. Fang, Effect of phase transition on optical and photoluminescence properties of nano- $\text{MgWO}_4$  phosphor prepared by a gamma-ray irradiation assisted polyacrylamide gel method, *J. Mater. Sci.: Mater. Electron.*, 2019, **30**, 15744–15753.



41 F. Grote, R. S. Kühnel, A. Balducci and Y. Lei, Template assisted fabrication of free-standing  $\text{MnO}_2$  nanotube and nanowire arrays and their application in supercapacitors, *Appl. Phys. Lett.*, 2014, **104**, 053904.

42 A. Nadort, J. Zhao and E. M. Goldys, Lanthanide upconversion luminescence at the nanoscale: fundamentals and optical properties, *Nanoscale*, 2016, **8**, 13099–13130.

43 M. Pollnau, D. R. Gamelin, S. R. Lüthi, H. U. Güdel and M. P. Hehlen, Power dependence of upconversion luminescence in lanthanide and transition-metal-ion systems, *Phys. Rev. B: Condens. Matter Mater. Phys.*, 2000, **61**, 3337.

44 M. K. Mahata, T. Koppe, T. Mondal, C. Brüsewitz, K. Kumar, V. K. Rai, U. Vetter, *et al.* Incorporation of  $\text{Zn}^{2+}$  ions into  $\text{BaTiO}_3$ :  $\text{Er}^{3+}/\text{Yb}^{3+}$  nanophosphor: an effective way to enhance upconversion, defect luminescence and temperature sensing, *Phys. Chem. Chem. Phys.*, 2015, **17**, 20741–20753.

45 M. Mondal and V. K. Rai,  $\text{Ho}^{3+}\text{-Yb}^{3+}$ :  $\text{YMoO}_4$  core@ shell nanoparticles for enhanced visible upconversion and security applications, *J. Alloys Compd.*, 2018, **750**, 304–311.

46 Z. T. Chen, E. H. Song, M. Wu, S. Ding, S. Ye and Q. Y. Zhang, Bidirectional energy transfer induced single-band red upconversion emission of  $\text{Ho}^{3+}$  in  $\text{KZnF}_3$ :  $\text{Mn}^{2+}$ ,  $\text{Yb}^{3+}$ ,  $\text{Ho}^{3+}$  nanocrystals, *J. Alloys Compd.*, 2016, **667**, 134–140.

47 G. Bilir, G. Ozen, M. Bettinelli, F. Piccinelli, M. Cesaria and B. Di Bartolo, Broadband Visible Light Emission From Nominally Undoped and  $\text{Cr}^{3+}$  Doped Garnet Nanopowders, *IEEE Photonics J.*, 2014, **6**, 1–11.

48 Y. Zhu, W. Xu, C. Li, H. Zhang, B. Dong, L. Xu, H. Song, *et al.* Broad white light and infrared emission bands in  $\text{YVO}_4$ :  $\text{Yb}^{3+}$ ,  $\text{Ln}^{3+}$  ( $\text{Ln}^{3+} = \text{Er}^{3+}$ ,  $\text{Tm}^{3+}$ , or  $\text{Ho}^{3+}$ ), *Appl. Phys. Express*, 2012, **5**, 092701.

49 L. Marciniak, W. Strek, D. Hreniak and Y. Guyot, Temperature of broadband anti-Stokes white emission in  $\text{LiYbP}_4\text{O}_{12}$ :  $\text{Er}$  nanocrystals, *Appl. Phys. Lett.*, 2014, **105**, 173113.

50 X. Chen, W. Xu, Y. Zhu, P. Zhou, S. Cui, L. Tao, H. Song, *et al.*  $\text{Nd}_2\text{O}_3/\text{Au}$  nanocomposites: upconversion broadband emission and enhancement under near-infrared light excitation, *J. Mater. Chem. C*, 2014, **2**, 5857–5863.

51 W. Xu, X. Min, X. Chen, Y. Zhu, P. Zhou, S. Cui, H. Song, *et al.*  $\text{Ag-SiO}_2\text{-Er}_2\text{O}_3$  nanocomposites: Highly effective upconversion luminescence at high power excitation and high temperature, *Sci. Rep.*, 2014, **4**, 5087.

52 D. Chen, Y. Zhou and J. Zhong, A review on  $\text{Mn}^{4+}$  activators in solids for warm white light-emitting diodes, *RSC Adv.*, 2016, **6**(89), 86285–86296.

53 *Upconverting Nanoparticles: From Fundamentals to Applications*, ed. V. K. Rai, John Wiley & Sons, 2022.

54 K. Sankarasubramanian, B. Devakumar, G. Annadurai, L. Sun, Y. J. Zeng and X. Huang, Novel  $\text{SrLaAlO}_4$ :  $\text{Mn}^{4+}$  deep-red emitting phosphors with excellent responsiveness to phytochrome PFR for plant cultivation LEDs: synthesis, photoluminescence properties, and thermal stability, *RSC Adv.*, 2018, **8**, 30223–30229.

55 T. Hu, H. Lin, Y. Cheng, Q. Huang, J. Xu, Y. Gao, Y. Wang, *et al.* A highly-distorted octahedron with a C 2v group symmetry inducing an ultra-intense zero phonon line in  $\text{Mn}^{4+}$ -activated oxyfluoride  $\text{Na}_2\text{WO}_2\text{F}_4$ , *J. Mater. Chem. C*, 2017, **5**, 10524–10532.

56 Y. Lv, Y. Jin, T. Sun, J. Su, C. Wang, G. Ju, Y. Hu, *et al.* Visible to NIR down-shifting and NIR to visible upconversion luminescence in  $\text{Ca}_{14}\text{Zn}_6\text{Ga}_{10}\text{O}_{35}$ :  $\text{Mn}^{4+}$ ,  $\text{Ln}^{3+}$  ( $\text{Ln} = \text{Nd}$ ,  $\text{Yb}$ ,  $\text{Er}$ ), *Dyes Pigm.*, 2019, **161**, 137–146.

57 J. Grigorjevaite and A. Katelnikovas, Up-Converting  $\text{K}_2\text{Gd}(\text{PO}_4)(\text{WO}_4)$ : 20%  $\text{Yb}^{3+}$ ,  $\text{Ho}^{3+}$  Phosphors for Temperature Sensing, *Materials*, 2023, **16**, 917.

58 M. Prasad and V. K. Rai, Coactivated cyan emitting phosphors in optical thermometry using thermally and non-thermally coupled levels, *Mater. Res. Bull.*, 2022, **160**, 112116.

59 B. Bondzior, D. Stefańska, T. H. Q. Vũ, N. Miniajlk-Gawel and P. J. Dereń, Red luminescence with controlled rise time in  $\text{La}_2\text{MgTiO}_6$ :  $\text{Eu}^{3+}$ , *J. Alloys Compd.*, 2021, **852**, 157074.

60 M. Prasad, M. Mondal, L. Mukhopadhyay, S. Pattnaik and V. K. Rai, Photoluminescence investigation in tungstate-based materials, *Mater. Today: Proc.*, 2021, **46**, 6388–6391.

61 Z. Jia and M. Xia, Blue-green tunable color of  $\text{Ce}^{3+}/\text{Tb}^{3+}$  coactivated  $\text{NaBa}_3\text{La}_3\text{Si}_6\text{O}_{20}$  phosphor via energy transfer, *Sci. Rep.*, 2016, **6**, 1–9.

62 W. H. Du, N. Zhang, N. Z. Zhuo, L. Y. Xie, T. Jiang, Y. H. Zhu, H. B. Wang, *et al.* Photoluminescence properties and energy transfer of apatite-type  $\text{Sr}_3\text{LaNa}(\text{PO}_4)_3\text{F}$ :  $\text{Ce}^{3+}$ ,  $\text{Tb}^{3+}$  phosphors, *Mater. Res. Express*, 2019, **6**, 126209.

63 K. Sankarasubramanian, B. Devakumar, G. Annadurai, L. Sun, Y. J. Zeng and X. Huang, Novel  $\text{SrLaAlO}_4$ :  $\text{Mn}^{4+}$  deep-red emitting phosphors with excellent responsiveness to phytochrome PFR for plant cultivation LEDs: synthesis, photoluminescence properties, and thermal stability, *RSC Adv.*, 2018, **8**, 30223–30229.

64 L. Mukhopadhyay and V. K. Rai, Thermally stable red emitting xenotime phosphate nanophosphors for displays, *Mater. Res. Bull.*, 2020, **121**, 110628.

65 H. Chen, H. Lin, Q. Huang, F. Huang, J. Xu, B. Wang, Y. Wang, *et al.* A novel double-perovskite  $\text{Gd}_2\text{ZnTiO}_6\text{:Mn}^{4+}$  red phosphor for UV-based w-LEDs: structure and luminescence properties, *J. Mater. Chem. C*, 2016, **4**, 2374–2381.

66 S. Pattnaik and V. K. Rai, Tailoring of upconversion luminescence of  $\text{Al}^{3+}$  engineered titanate phosphor for non-invasive thermometry, *Methods Appl. Fluoresc.*, 2022, **10**, 034002.

67 B. Henderson and G. F. Imbusch, *Optical spectroscopy of inorganic solids*, Oxford University Press, 2006, vol. 44.

68 T. Senden, R. J. van Dijk-Moes and A. Meijerink, Quenching of the red  $\text{Mn}^{4+}$  luminescence in  $\text{Mn}^{4+}$ -doped fluoride LED phosphors, *Light: Sci. Appl.*, 2018, **7**, 1–13.

69 J. Dutta and V. K. Rai, Zirconia based  $\text{Ho}^{3+}\text{-Yb}^{3+}$  codoped upconverting nanophosphors for green light emitting devices applications, *Methods Appl. Fluoresc.*, 2018, **6**, 025003.

